ELSEVIER

Journal of Nuclear Materials 317 (2003) 1–12

journal of nuclear materials

www.elsevier.com/locate/jnucmat

Effect of β phase, precipitate and Nb-concentration in matrix on corrosion and oxide characteristics of Zr–*x*Nb alloys

Yong Hwan Jeong [a,*], Hyun Gil Kim [a,b], To Hoon Kim [b]

[a] *Nuclear(Zirconium) Fuel Cladding Team, Korea Atomic Energy Research Institute, P.O. Box 105, Yusong Daejeon 305-600, South Korea*

[b] *Department of Materials Sciences and Engineering, Yonsei University, Sinchon-dong 134, Seodaemoon-ku, Seoul 120-749, South Korea*

Received 25 June 2001; accepted 25 November 2002

Abstract

The corrosion test and oxide characterization were performed on the specimens having different Nb-content in the range of 0–5 wt%. The specimens were heat-treated at 570 °C for 500 h to get the $\alpha + \beta_{Nb}$ phase and at 640 °C for 10 h to get the $\alpha + \beta_{Zr}$ phase after β-quenching. The corrosion tests were carried out at 360 °C. In the low Nb-contents of 0.1–0.2 wt% where Nb was soluble in the matrix without the formation of Nb-containing precipitates or β phase, the samples showed the excellent corrosion resistance and their corrosion resistance was not affected by heat-treatment. The corrosion resistance was improved by the stabilization of tetragonal ZrO_2 and columnar oxide structure when all added Nb was soluble in the matrix to equilibrium concentration. In the high Nb-contents of 1.0–5.0 wt%, the corrosion rate was very sensitive to the annealing condition. The transformation of oxide crystal structure from tetragonal ZrO_2 to monoclinic ZrO_2 and oxide microstructure from columnar to equiaxed structure was accelerated in the samples having β_{Zr} phase, while retarded in the sample having β_{Nb} phase. This means that the formation of β_{Nb} phase resulted in the reduction of Nb concentration in the α matrix, thus the corrosion resistance was enhanced with the formation of β_{Nb} phase. From the corrosion test and oxide characterization, it is suggested that the equilibrium concentration of Nb in the α matrix would be a more dominant factor to enhance the corrosion resistance than the Nb-containing precipitates, supersaturated Nb, and β phase (β_{Nb} or β_{Zr}).

PACS: 81.65.M; 81.65.K; 42.81.B

1. Introduction

Zircaloy-4 alloy has been used as nuclear fuel cladding materials for several decades without any significant problems in pressurized water reactor. However more advanced Zr-based alloys are recently required for the severe operating condition such as higher burn-up, increased operation temperature, and high pH operation. As a substitute for Zircaloy-4, several new Zr alloys such as Zirlo (Zr–1.0Nb–1.0Sn–0.1Fe) [1], M5 (Zr–1Nb–O) [2] and NDA (Zr–0.1Nb–1.0Sn–0.27Fe–0.16Cr) [3] were developed and are being tested in-reactor. Like this, most new Zr alloys that are being developed contain the Nb element. However, it is reported that the corrosion behavior of Nb-containing Zr alloy is very sensitive to the microstructures that could be changed by heat treatment.

Up to now, the correlation between microstructural changes and corrosion behaviors in Zr–Nb binary alloys, in particular Zr–2.5Nb alloy, have been investigated by many workers [4–11]. It is reported that the martensitic structure where all the added Nb is supersaturated in the matrix and β_{Zr}(~20 wt% Nb) phase accelerates the oxidation of Zr alloy, while β_{Nb} phase retards the oxidation of Zr alloy [4,5]. It is known that

* Corresponding author. Tel.: +82-42 868 2322; fax: +82-42 862 0432.

E-mail address: yhjeong@kaeri.re.kr (Y.H. Jeong).

0022-3115/03/$ - see front matter
doi:10.1016/S0022-3115(02)01676-8

β_{Nb} phase is produced by aging of quenched Zr–Nb alloy having martensitic structure below monotectoid temperature (610 °C) [6,7], or by the decomposition of β_{Zr} phase to $\alpha_{Zr} + \beta_{Nb}$ phases when β_{Zr} phase is annealed [8,9]. Also, Urbanic and Gilbert [4] reported that the corrosion resistance was enhanced with precipitation of β_{Nb} phase in Zr–2.5Nb pressure tube under irradiation condition. However, these studies were mainly focused on the Zr–2.5wt%Nb alloy that is being used as a pressure tube material for CANDU-PHW reactors. Isobe and Matsuo [10] reported that the corrosion resistance of Zircaloy-4 was improved by small Nb addition to it. Also, many studies have performed to improve the corrosion resistance of Zr-based alloys with changing not only their Nb-content but also their microstructure control through heat-treatment. However, most studies were mainly focused on the corrosion behavior or microstructure. The correlation between oxide characteristics and microstructure or microchemistry such as β phases, Nb-containing precipitates, and soluble Nb in matrix is not well understood in Zr–Nb alloys.

Thus, for better understanding the correlation between microstructure and corrosion behavior or oxide chracteristics, it is necessary to do the systematic study with the variation of Nb-content and annealing condition in Zr–Nb binary alloys. Therefore, in this study, the specimens having different microstructure were prepared with the variation of Nb-content and annealing condition. And the corrosion test, the microstructural study, and the oxide characterization for the specimens were performed to investigate the effect of the soluble Nb-content, β phase, and precipitates on the corrosion resistance and to identify the main controlling factor for the enhancement of corrosion resistance in Nb-containing Zr alloys.

2. Experimental procedure

Zirconium alloy ingots having different Nb-content in the range of 0–5.0 wt% were prepared by vacuum arc remelting method with sponge zirconium from Wah Chang Albany and high purity (99.99%) niobium. The low Nb-contents of 0–0.3 wt% were selected to investigate the effect of soluble Nb in the matrix on the corrosion. The alloys that have the medium Nb-contents of 0.3–1.0 wt% and the high Nb-content of 1.0–5 wt% were prepared for studying the effect of the Nb precipitates and the β phase on the corrosion, respectively. These ingots were then rolled to approximately 1.0 mm thickness sheets. These rolled sheet specimens were β-quenched following heating at 1050 °C for 20 min in order to remove the annealing effect during the manufacturing process and then annealed at 570 °C for 500 h to obtain the β_{Nb} phase and at 640 °C for 10 h to obtain the β_{Zr} phase as shown in Table 1 and Fig. 1. The samples annealed at 570 and 640 °C were directly quenched into water to give the fast cooling rate.

The specimens for autoclave corrosion testing were polished with SiC paper to remove surface contaminant. The corrosion test was performed in a static autoclave with distilled water under the condition of 360 °C and 18.9 MPa according to the procedure of ASTM G2. The microstructural observation and the analysis for the precipitates were performed using the polarized optical microscopy and transmission electron microscopy. The observation of optical microstructure was performed for the perpendicular section to the rolling direction of specimens, and the specimens were etched with a solution containing 10 vol.% HF, 45 vol.% HNO_3 and 45 vol.% H_2O. Thin foils for transmission electron microscopy of matrix were prepared by grinding down to 70 μm in thickness and then electrolytically polished with a mixed solution of 90 vol.% ethanol and 10 vol.% perchloric acid using twin-jet electro-polisher at −40 °C. The analysis of chemical composition of the precipitates was performed using a TEM equipped with energy dispersive X-ray spectroscopy (EDS), and the area fraction of second phase was calculated using the image analyzer from the TEM photographs.

The oxide characteristics were investigated by using synchrotron X-ray scattering, low angle XRD, and TEM. The synchrotron X-ray scattering experiments were carried out at beamline 5C2 at Pohang Light Source in Korea for the corroded specimens having the equal weight gain of 20 mg/dm^2. The incident beam angle was 2° on all oxide samples for the analysis of synchrotron X-ray scattering and low angle XRD. For the TEM observation on the oxide, the sections with oxide on the corroded samples were glued to each other and they were sliced in the thickness of about 300 μm for the perpendicular direction to the oxide/metal interface.

Table 1
Chemical composition of Zr–*x*Nb alloy and annealing condition

Alloy	Heat-treatment
Zr–*x*Nb 1[a] – (x = 0.05, 0.1, 0.2, 0.3, 0.4, 0.5, 0.6, 0.8, 1.0, 1.5, 2.0, 3.0, 5.0 wt%) 2[a] – O: 500 ppm, Fe: 400 ppm, Cr < 50 ppm, C < 36 ppm, Si < 10 ppm	(a) 570 °C × 500 h ($\alpha + \beta_{Nb}$ region) (b) 640 °C × 10 h ($\alpha + \beta_{Zr}$ region)

[a] Compositions of alloying elements are nominal values.

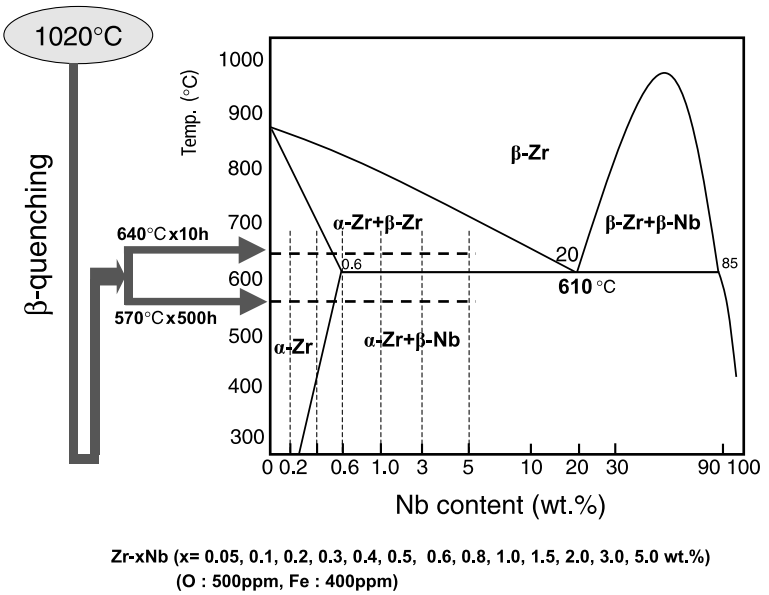

Fig. 1. Experimental procedure showing the annealing condition and Nb-content.

The sliced specimens were mechanically polished until their thickness became 20–30 μm and then finally prepared by an ion-milling.

3. Results and discussion

3.1. Characteristics of microstructure with Nb-content and annealing condition

Fig. 2 shows the optical microstructure of Zr–*x*Nb alloys with the variation of Nb-contents and annealing conditions. The optical microstructures were changed depending on the Nb-content in both annealing conditions. Even though the samples were annealed at 570 and 640 °C for long time, β-quenched structures were maintained without the significant change of plate or grain shape. As the Nb-content increased, the microstructure was getting fine, in particular in the Nb-content more than 2.0 wt%. It is known that M_S temperature is affected by the amount of Nb-content, and M_S temperature is decreased with increasing Nb-content and cooling rate in Zr–Nb alloy system [11,12]. Thus it is considered that the variation of microstructure with Nb-content resulted from the different M_S temperature even in the same cooling rate. In other words, it means that M_S temperature of samples having Nb more than 2.0 wt% is so low as to produce the martensitic structure. Even though the effect of annealing on the microstructure change was not clearly observed in both conditions, however it is expected that the substructures such as precipitates and dislocation would be changed in these annealed samples. To investigate the microstructure more clearly, TEM observation was performed for the samples annealed at 570 and 640 °C.

Fig. 3 shows the TEM micrographs of the Zr–*x*Nb alloys annealed at 570 °C for 500 h, which was applied to produce the $(\alpha + \beta_{Nb})$ phase. The type, distribution, and volume fraction of second phase particle were changed with increasing the Nb-content. In Zr–0.1Nb alloy (Fig. 3(a)), the Zr_3Fe type precipitate was observed at grain boundary even though Fe was not added in the sample. The formation of Zr_3Fe type precipitate resulted from Fe in sponge zirconium. The maximum solubility of Fe in Zr–Fe alloy is known to be about 200 ppm [13]. The Fe-content in sponge zirconium used in this study was 420 ppm. Thus, most Fe in sponge Zr would be precipitated as Fe-containing precipitates. In Zr–0.3Nb (Fig. 3(b)) and Zr–0.5Nb alloys (Fig. 3(c)), $Zr(NbFe)_2$ type precipitates having the chemical composition of $Zr_{0.4}Nb_{0.4}Fe_{0.2}$ were observed at grain boundaries. The precipitates were identified to be of $Zr(NbFe)_2$ type of hexagonal structure by selected area diffraction (SAD) analysis. The $(ZrNb)_3Fe$ type precipitates of orthorhombic structure were not found in these alloys. The Nb in Zr is known to have the maximum solubility of 0.6 wt% by Cox and Lundin and as β-stabilizer [14]. However, Nb-containing precipitates were observed on the Zr–0.3Nb alloy containing 520 ppm O and 420 ppm Fe in spite of the low Nb-contents of 0.3 wt% alloys. This means that Nb solubility in Zr–*x*Nb binary alloy used in this study would be lower than 0.3 wt% due to the β-stabilizer like Fe. The $\beta_{enriched}$ phase containing 30–50 wt% Nb was observed in Zr–0.8Nb alloy that was

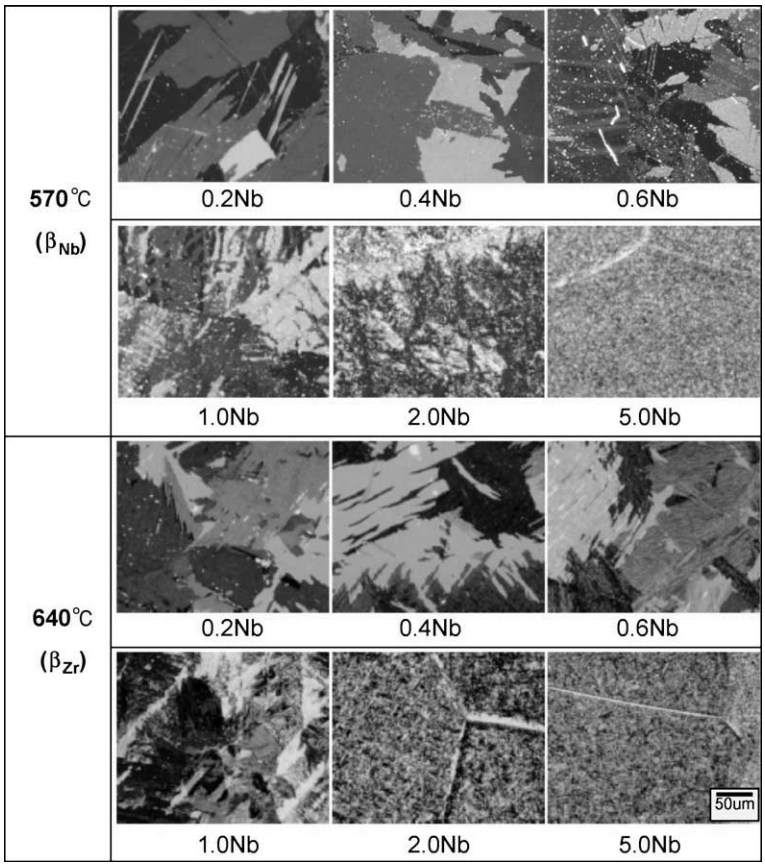

Fig. 2. Optical microstructures of Zr–*x*Nb alloys with the variation of Nb-content and annealing condition.

annealed at 570 °C for 500 h. This resulted from either the annealing time is not enough to form β_{Nb} in 0.8 wt% Nb or Nb-content is not enough to form β_{Nb} in this annealing condition. The β_{Nb} phases were observed in Zr with 1.0 and 3.0 Nb alloy having the high Nb-content.

Fig. 4 shows the TEM micrographs of the Zr–*x*Nb alloys annealed at 640 °C for 10 h, which was applied to produce the $\alpha + \beta_{Zr}$ phase. In the range of 0.1–5.0Nb, the type, distribution, and shape of precipitate in the sample annealed at 640 °C for 10 h were very similar to those in the sample annealed at 570 °C for 500 h. However, in the high Nb-containing alloys annealed at $\alpha + \beta_{Zr}$ region, the characteristic of the second phase was different from that in the alloy annealed at $\alpha + \beta_{Nb}$ region. The microstructure was lamellar structure showing the β_{Zr} phase at plate boundary and the area fraction of second phase was higher than that in the samples annealed at $\alpha + \beta_{Nb}$ region.

Table 2 shows the summary of the precipitates and β phase investigated in this study. The characteristics of the second phase were changed with the annealing condition and Nb-content. It was found that the β_{Nb} phase having round shape mainly formed in the alloy annealed at 570 °C of the $\alpha + \beta_{Nb}$ region, and the β_{Zr} phase having elongated shape in the alloy annealed at 640 °C of the $\alpha + \beta_{Zr}$ region. The relative volume fraction of $Zr(NbFe)_2$ type precipitates would be decreased with increasing Nb-content because the solubility of Fe increased in the β phase and Fe elements were also more dispersed at the increased grain boundaries of high Nb-content alloys than that of low Nb-content alloys as reported by Perovic et al. [15].

3.2. Corrosion characteristics with Nb-content and annealing condition

Fig. 5 shows that the corrosion behavior of Zr–*x*Nb binary alloys with Nb-content and annealing condition. In the samples annealed at 570 °C as shown in Fig. 5(a), the corrosion kinetics of the alloys was the cubic rate in the early stage of corrosion and then nearly saturated after 30 days up to 90 days. The transitions of corrosion rate were not observed on the all specimens even after exposure time of 90 days. In the samples annealed at 640 °C as shown in Fig. 5(b), the corrosion behaviors of the low Nb-containing alloys were nearly similar to those of

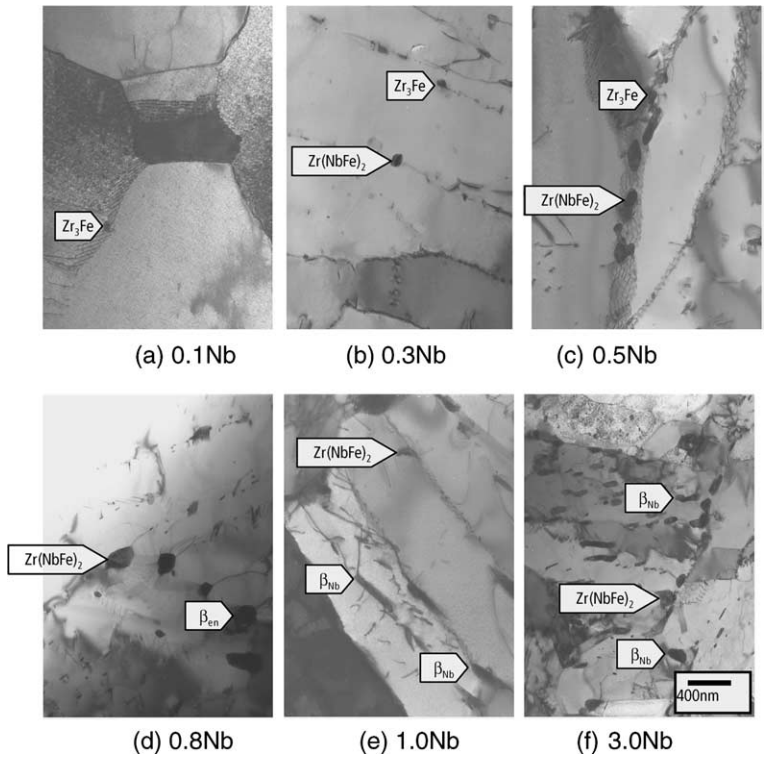

Fig. 3. TEM micrographs of Zr–*x*Nb alloys annealed at 570 °C for 500 h with varation of Nb-content.

specimens annealed at 570 °C, but the high Nb-containing alloys showed higher corrosion rate and earlier acceleration of corrosion rates than the alloys annealed at 570 °C.

Fig. 6 shows the variation of weight gain of Zr–*x*Nb alloys with different heat treatment as a function of Nb-content. It was clearly revealed that the corrosion rate of Zr–*x*Nb alloys was significantly different depending on the Nb-content and annealing condition. The corrosion behavior of Zr–*x*Nb alloy was classified into three groups (region A, B, and C) with the Nb-content. From above results, it is expected that the corrosion behavior of Nb-containing alloys would be affected by the content of soluble Nb in the matrix, Nb-containing precipitate, and β phase. In the range of low Nb-content from 0 to 0.3 wt% identified as region A, the weight gain slightly decreased up to 0.1–0.2 wt% in Nb-content but increased again with increasing the Nb-content. In this region up to 0.2 wt% Nb, Nb-containing precipitate and β phase were not observed by TEM observation and the corrosion resistance was not affected by the heat-treatment maintaining the low weight gain. Therefore, it is suggested that the corrosion rate in this region would be controlled by the soluble Nb in the matrix. This means that the equilibrium concentration of Nb in the matrix enhance the corrosion resistance of Zr–*x*Nb alloys. In the range of medium Nb-content from 0.3 to 1.0 wt% identified as region B, the weight gain gradually increased with increasing Nb-content showing the effect of heat-treatment. It was found from TEM study that the Nb-containing precipitates [$Zr(NbFe)_2$-type] were observed even in the alloys having 0.3 wt% Nb. It is considered that Nb-containing precipitates would control the corrosion rate in this region resulting in the corrosion acceleration.

In the range of high Nb-content from 1.0 to 5.0 wt% identified as the region C, the corrosion rate of the alloys were very sensitive to the heat-treatment and they showed the quite different corrosion behavior depending on the annealing condition. The corrosion rate of the sample annealed at 570 °C with formation of the β_{Nb} phase was much lower than that of sample annealed at 640 °C with formation of the β_{Zr} phase. Thus, it is thought that β_{Nb} phase is beneficial to the corrosion while β_{Zr} phase is detrimental to the corrosion. However, it is not clear whether β_{Nb} phase is the main cause for increasing the corrosion resistance of Zr–*x*Nb alloy because the formation of β_{Nb} phase results in the reduction of Nb-concentration in the matrix. Therefore, it is thought that the corrosion resistance would be enhanced by the reduction of Nb concentration in the matrix with formation of β_{Nb} phase containing 80 wt% Nb. The high corrosion rate in the sample annealed at 640 °C would be related to the high Nb concentration in

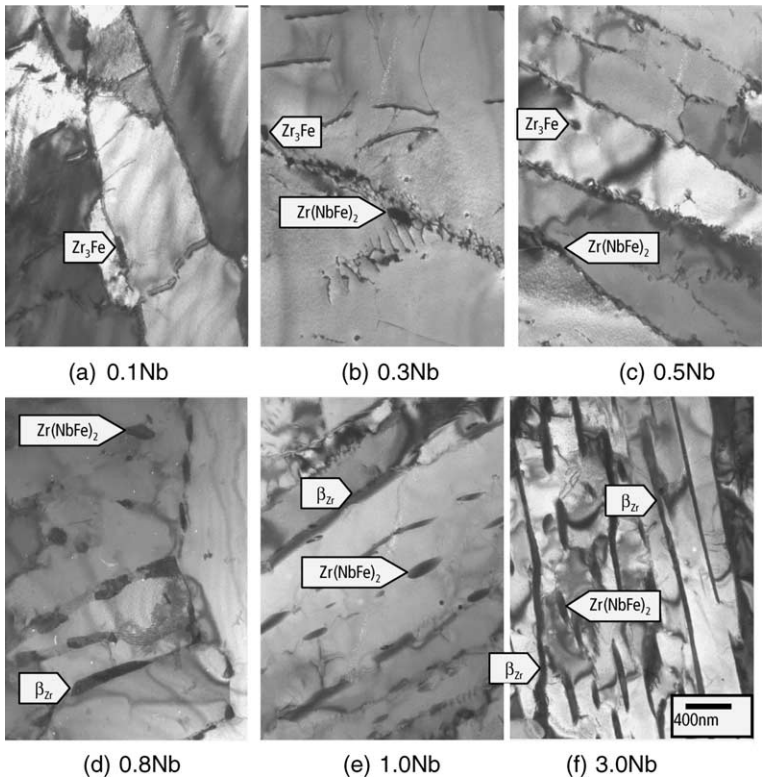

Fig. 4. TEM micrographs of Zr–*x*Nb alloys annealed at 640 °C for 10 h with varation of Nb-content.

Table 2
Summery of precipitate characteristics of Zr–*x*Nb alloys

Nb-content (wt%)		0.1	0.3	0.5	0.8	1.0	3.0
570 °C (β_{Nb})	Type	•Zr_3Fe	○Zr_3Fe	○Zr_3Fe	–	–	–
		–	•$Zr(NbFe)_2$	•$Zr(NbFe)_2$	•$Zr(NbFe)_2$	○$Zr(NbFe)_2$	○$Zr(NbFe)_2$
		–	–	–	○β_{en}	•β_{en}, β_{Nb}	•β_{en}, β_{Nb}
	Distribution	Grain boundary	Grain boundary	Grain boundary	In α-grain and grain-boundary	Plate boundary	In α-grain and plate-boundary
640 °C (β_{Zr})	Type	•Zr_3Fe	○Zr_3Fe	○Zr_3Fe	–	–	–
		–	•$Zr(NbFe)_2$	•$Zr(NbFe)_2$	•$Zr(NbFe)_2$	○$Zr(NbFe)_2$	○$Zr(NbFe)_2$
		–	–	–	○β_{Zr}	•β_{Zr}	•β_{Zr}
	Distribution	Grain boundary	Grain boundary	In α-grain and grain-boundary	In α-grain and grain-boundary	Plate boundary	Plate boundary

•: Major; ○: minor.

the matrix due to the short annealing time and the contribution of high corrosion rate of β_{Zr} phase containing 20 wt% Nb.

To analyze the supersaturated or soluble Nb concentration in matrix, EDS analysis was performed for all the specimens. It was not successful to analyze the exact Nb concentration in matrix owing to the limited resolution of EDS. However, it can be expected that in the samples having Nb-content less than 0.3 wt%, the Nb would be soluble in the matrix without the supersaturation and in range of 0.3–0.8 wt%, the supersaturated Nb concentration would be increased with increasing the Nb-content. In the alloy having Nb-content more than 1.0 wt%, the sample annealed at 640 °C would have higher Nb concentration in the matrix than the sample annealed at 570 °C. And the Nb concentration in matrix

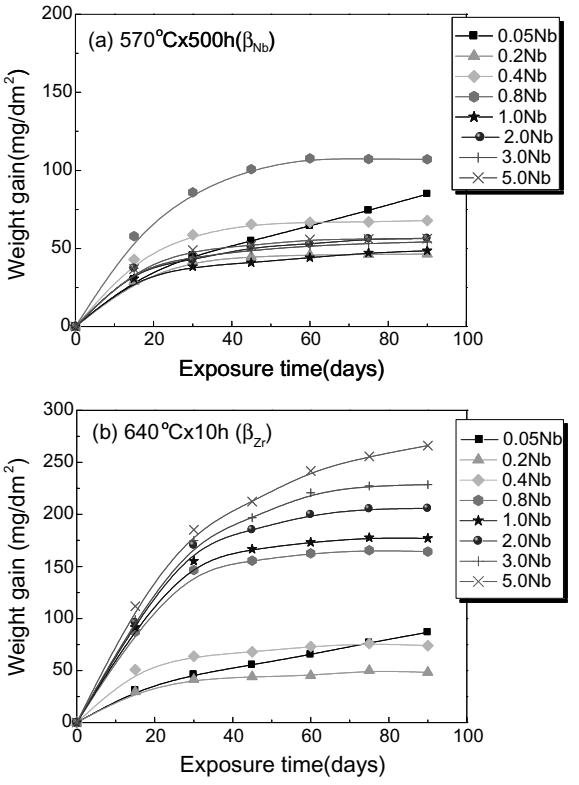

Fig. 5. Corrosion behaviors of Zr–xNb alloys in water at 360 °C. (a) 570 °C × 500 h and (b) 640 °C × 10 h

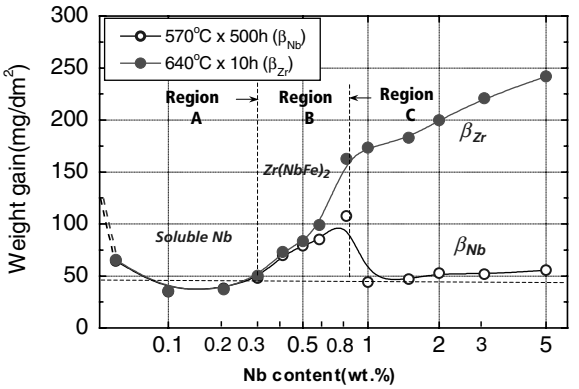

Fig. 6. Corrosion behaviors of Zr–xNb alloys with varation of Nb-content at 360 °C for 60 days.

of the sample annealed at 570 °C would be similar to the equilibrium concentration of Nb.

Therefore, the corrosion resistance with Nb-content and annealing condition would have close relationship with the concentration of soluble and supersaturated Nb in the matrix. In the samples having 1.0–5.0 wt% Nb, even though the volume fraction of β_{Nb} phase increased with increasing Nb-content, their weight gains were nearly constant and were similar to those in the samples having 0.1–0.3 wt% Nb. This means that the main controlling factor of corrosion resistance would be Nb concentration in the α matrix. In a previous study [16], the effect of supersaturated Nb concentration on the corrosion of Zr–xNb alloys was investigated with variation of cooling rate and Nb-contents. It was already reported that the supersaturated Nb had accelerated the corrosion rate of Zr–xNb binary alloys.

3.3. Oxide characterization by synchrotron X-ray scattering and low angle XRD

Pilling–Bedworth (PBW) ratio means volume ratio of metallic oxide versus metal, and PBW ratio of ZrO_2/Zr is as high as 1.56. So the high compressive stress due to volume expansion accompanied by formation of oxide is applied to the oxide formed in the early corrosion. In the early stage of corrosion, the plenty of tetragonal ZrO_2 that is meta-stable phase and has protective property is formed. However, as the oxidation is getting progressed, the protective tetragonal ZrO_2 is transformed to monoclinic ZrO_2 having non-protective property. It is known that the corrosion is accelerated by this change of oxide structure [17].

Fig. 7 shows the crystallography of oxide identified by synchrotron X-ray scattering and XRD for the Zr–0.3Nb alloy having the weight gain of about 20 mg/dm^2. Even though the incident beam angle was 2° in the analysis by both synchrotron X-ray scattering and XRD, the diffraction patterns were slightly different depending on the method for oxide analysis. In the conventional XRD, the low angle diffraction and local analysis are not easy because the beam size is too wide. But in the synchrotron X-ray scattering, it is possible to analyze the local area and to apply the low angle diffraction owing to small beam size (0.5 × 1 mm^2). In the low angle XRD, the major peaks of Zr matrix were observed, while in the synchrotron X-ray scattering, only the peaks from oxide were detected without the matrix peaks. In both methods, the (1 1 1) tetragonal ZrO_2 peak was observed in the vicinity of 30. Therefore, it is thought that the synchrotron X-ray scattering is more accurate technique to detect the crystallography of thin oxide film than the conventional low angle XRD.

Fig. 8 shows the synchrotron X-ray spectra of the oxides formed on the samples that annealed at 570 °C (Fig. 8(a)) and 640 °C (Fig. 8(b)). In the sample annealed at 570 °C, the measured peak intensity of tetragonal ZrO_2 was slightly higher in 0.3Nb alloy than 0.8Nb alloy. However, the intensities of monoclinic ZrO_2 were similar in the two alloys. Also, in the sample annealed at 640 °C, synchrotron X-ray scattering patterns were very similar to those in the sample annealed at 570 °C. However, the intensity of (0 0 2) monoclinic ZrO_2 in the

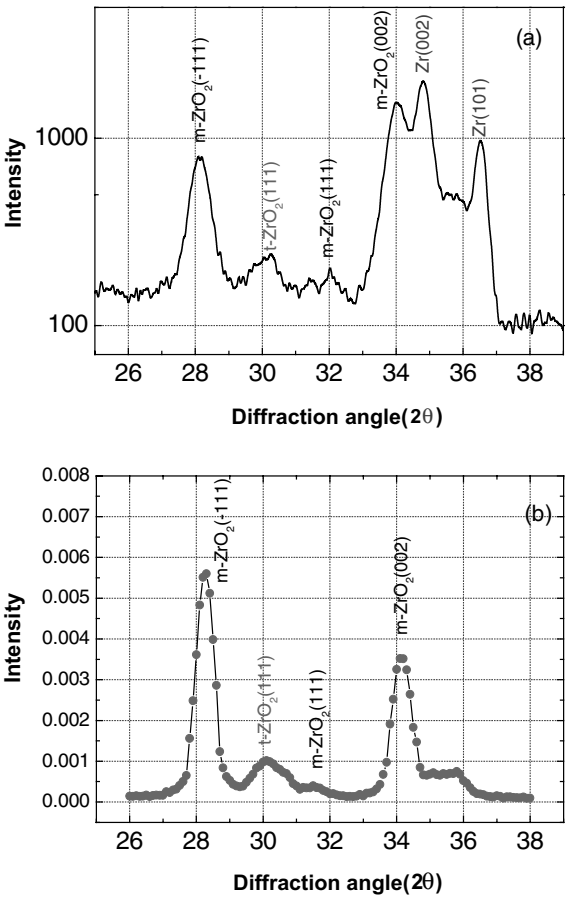

Fig. 7. Diffraction pattern of zirconium oxide having equal weight gain formed on Zr–0.3Nb alloys. (a) Conventional low angle XRD and (b) synchrotron X-ray scattering.

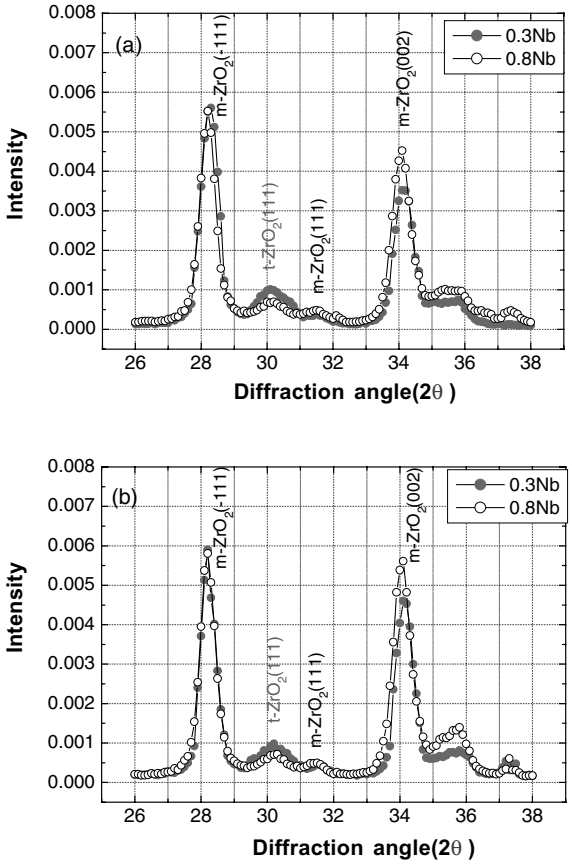

Fig. 8. Diffraction patterns of zirconium oxide formed at 360 °C by using synchrotron X-ray scattering. (a) β_{Nb}-annealing (570 °C × 500 h) and (b) β_{Zr}-annealing (640 °C × 10 h).

Zr–0.8Nb alloy that had shown the high corrosion rate was slightly higher than that in the Zr–0.3Nb alloy that had shown the low corrosion rate. Therefore, it is considered that the preferential growth of (0 0 2) monoclinic ZrO_2 has some relationship with the fast corrosion rate in the Zr–0.8Nb alloy. Fig. 9 shows the variation of volume fraction of tetragonal ZrO_2 measured by synchrotron X-ray scattering and low angle XRD with Nb-content in both annealing condition. The volume fraction of protective tetragonal ZrO_2 decreased with increasing Nb-content up to 0.8Nb regardless of the annealing condition, but more than 1.0 wt% Nb-content, it was changed depending on the annealing temperature. The volume fraction of tetragonal ZrO_2 increased again in the sample annealed at 570 °C to get the β_{Nb} phase while saturated in the sample annealed at 640 °C to get the β_{Zr} phase. This trend matched up to the result that the corrosion resistance of the Zr–Nb alloys having Nb in the range of 0.1–0.3 wt% was better than that of samples in the range of 0.3–0.8 wt% Nb, and the

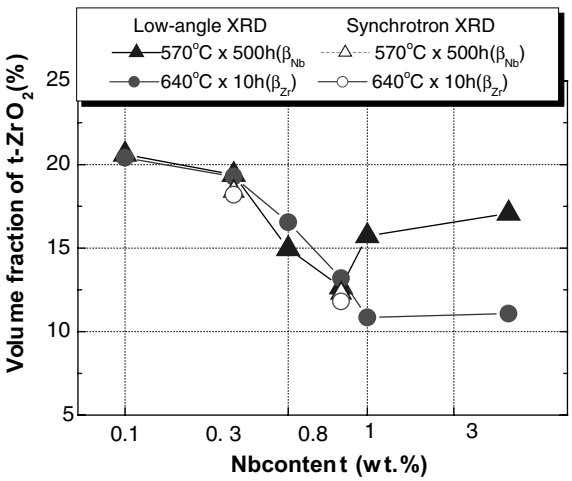

Fig. 9. Variation of volume fraction of tetragonal ZrO_2 with Nb-content for the same oxide thickness.

sample annealed at 570 °C showed higher corrosion resistance than the sample annealed at 640 °C.

3.4. Oxide characterization by TEM

Many workers have investigated the oxide characteristics by using TEM and SEM to understand corrosion mechanisms [18–20]. It was reported that the columnar oxide was beneficial while the equiaxed oxide was detrimental to the corrosion resistance. In this study, the observation on oxide microstructure by TEM was also performed for the Zr with 0.3, 0.8, and 3.0 Nb alloy annealed at 570 and 640 °C.

Fig. 10 shows the oxide microstructures in some Zr–*x*Nb alloys corroded to have almost equal weight gain of 20 mg/dm^2 at pre-transition. In the samples annealed at 570 °C, the microstructures of oxides were mostly a columnar structure even though they had different Nb-content. But in the samples annealed at 640 °C, the columnar structure was formed on the alloys having 0.3 and 0.8 wt% Nb-content while the equiaxed structure was formed on the alloys having 3.0 wt% Nb. This result well coincided with the fact that samples annealed at 570 °C showed better corrosion resistance than those annealed at 640 °C. It is expected that the different corrosion resistance with annealing condition would be related to the oxidation characteristics of β_{Zr} phase and β_{Nb} phase in the oxide during corrosion. Therefore, the change of second phase particle in the oxide was investigated.

Fig. 11 shows the oxide microstructure of sample having 3.0 wt% Nb-content annealed at 570 °C. It was found that the second phases (P1, P2, and P3) were still remained in the columnar oxide but their size was getting finer toward the surface. These second phases were analyzed to be composed of high Nb, low Zr, and low O as shown in EDS spectra and their crystal structures are of amorphous as shown in SAD pattern in Fig. 11. This means that the corrosion rate of the β_{Nb} phase was much lower than that of Zr matrix and the crystal structure of β_{Nb} phase was changed to amorphous during oxidation. Also, β_{Nb} phase did not accelerate the transformation of oxide microstructure from columnar to equiaxed structure.

Fig. 12 shows the oxide microstructure of the Zr–3.0Nb alloy annealed at 640 °C. As shown in Fig. 12(b), the oxidized β_{Zr} phase has a micro-equiaxed structure. Also, β_{Zr} phase accelerates the transformation of oxide microstructure from columnar to equiaxed at the interface between β_{Zr} phase and surrounding oxide. Therefore, it was thought that the β_{Zr} phase would have accelerated the oxide microstructure from the columnar to the equiaxed one and the oxide crystal structure from tetragonal ZrO_2 to monoclinic ZrO_2, while β_{Nb} phase did not affect the oxide transformation.

3.5. Oxidation characteristics of the simulated β phase

In order to investigate the oxidation characteristics of the simulated β_{Zr} phase and β_{Nb} phase, two kinds of samples were prepared as shown in Table 3. The X-ray analysis was performed on the manufactured specimens to check the exact crystal structure as shown in Fig. 13. It is known that β phase has only one phase of the β_{Nb} or the β_{Zr}. In the X-ray pattern, only single phase was observed in the simulated β_{Zr} phase and β_{Nb} phase without any peaks from α_{Zr}. Fig. 14 shows the corrosion behavior of the simulated β phase specimens at 360 °C in pressurized water. The weight gain of β_{Zr} phase was higher than that of β_{Nb} phase. From this result, it was

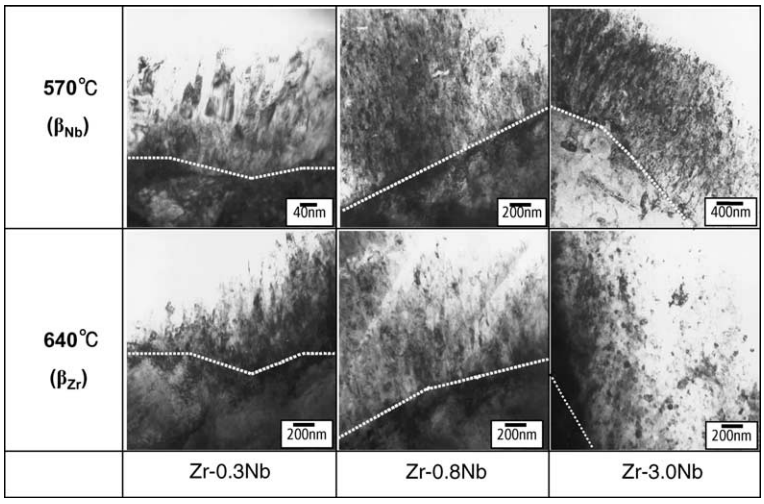

Fig. 10. Cross-sectional TEM micrographs of zirconium oxide at pre-transition in Zr–*x*Nb alloys with annealing condition and Nb-content.

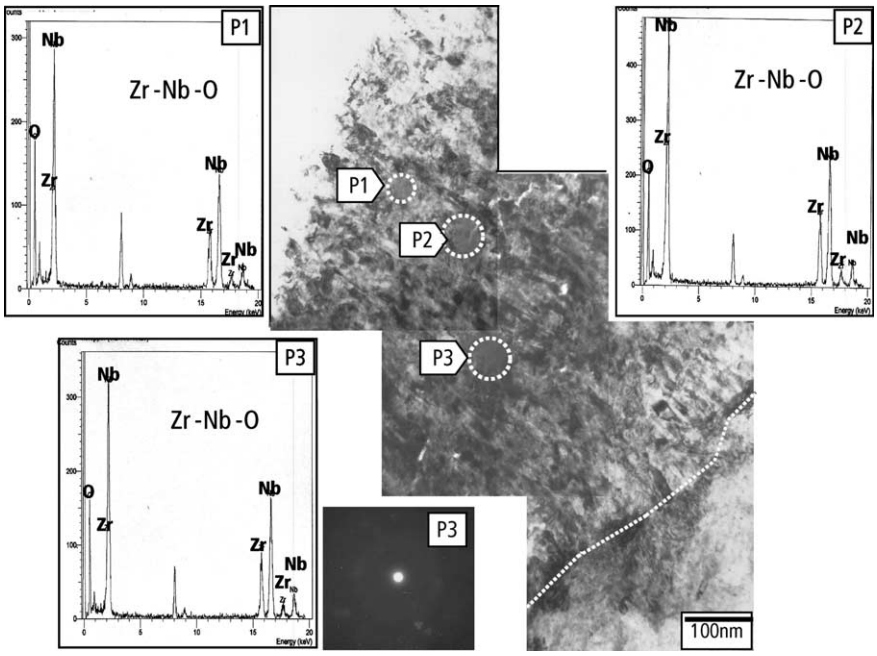

Fig. 11. Cross-sectional TEM micrographs and EDS spectra of zirconium oxide at pre-transition in Zr–3.0Nb alloy (β_{Nb}-annealing, 570 °C × 500 h).

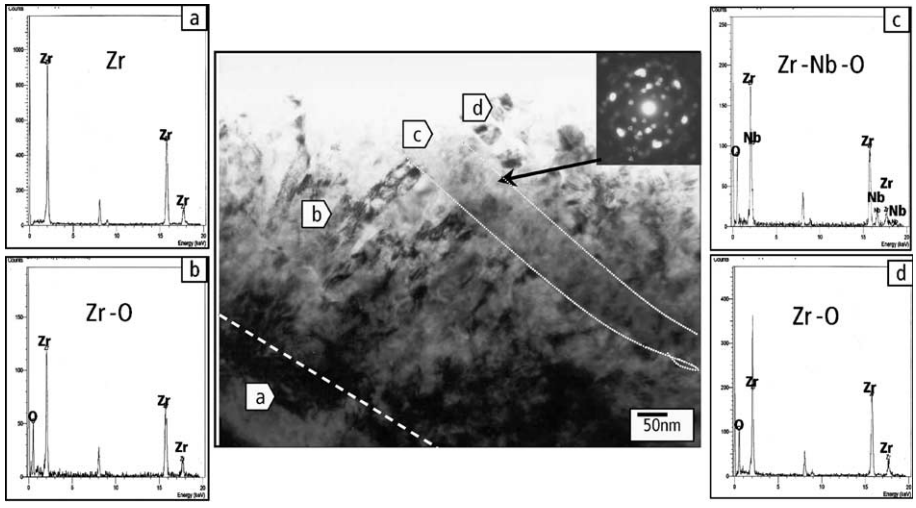

Fig. 12. Cross-sectional TEM micrographs and EDS spectra of zirconium-oxide at pre-transition in Zr–3.0Nb alloy (β_{Zr} annealing, 640 °C × 10 h).

Table 3
Alloy composition of simulated β_{Zr} and β_{Nb} phase

	640 °C (β_{Zr})	570 °C (β_{Nb})
Alloy composition	Zr: 80 wt% Nb: 20 wt%	Zr: 10 wt% Nb: 90 wt%
Heat-treatment	640 °C 10 h	570 °C 10 h

confirmed that the oxidation rate of β_{Zr} phase was slightly faster than that of β_{Nb} phase. The improvement of corrosion resistance in β_{Nb} phase was not so high. Improvement was just by about 25% compared with that of β_{Zr} phase. However, as shown in Fig. 6, the corrosion rate of samples that had been annealed at 640 °C to form β_{Zr} phase showed 3–4 times as high as that of samples annealed at 570 °C to form β_{Nb} phase. From these re-

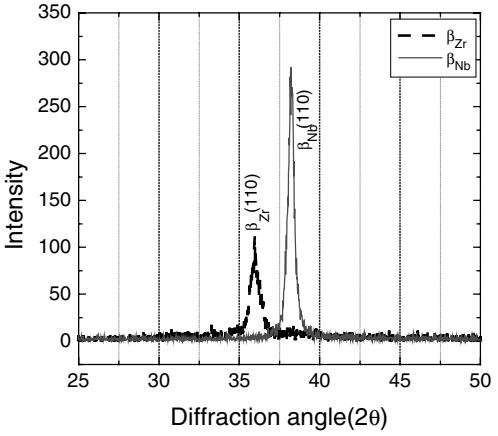

Fig. 13. XRD spectra of simulated β_{Zr} and β_{Zr} phase.

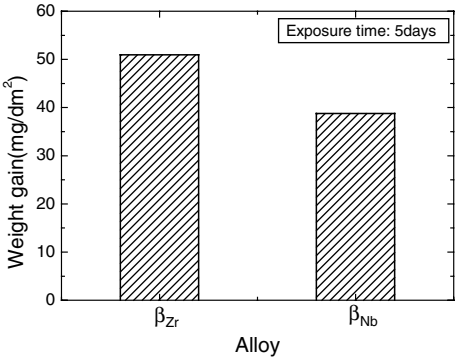

Fig. 14. Corrosion behavior of simulated β_{Zr} and β_{Nb} phase at 360 °C in water.

sults, it is thought that the oxidation characteristic of β_{Nb} phase itself was not the main cause for the superior corrosion resistance in the sample having β_{Nb} phase. The reduction of Nb concentration in the matrix with formation of β_{Nb} phase would be a main factor in the enhancement of corrosion resistance rather than β_{Nb} phase itself.

4. Conclusion

The corrosion behavior, microstructures, and oxide characteristics of Zr–*x*Nb alloys were quite different depending on the the Nb-content and annealing condition. In the alloys with low Nb-contents from 0 to 0.3 wt% (region A), the weight gain first decreased slightly up to 0.1–0.2 wt%, and then it went up again with increasing the Nb-content. In this region, Nb-contained precipitate and β phase were not observed in the alloys and their corrosion resistance was not affected by heat-treatment. It was observed from TEM and XRD studies that the oxides formed in pre-transition region were mainly consisted of columnar structures with high volume fraction of tetragonal ZrO_2. This means that the corrosion resistance was improved due to the stabilization of tetragonal ZrO_2 when Nb was soluble in the matrix to equilibrium concentration.

In the medium Nb-contents from 0.3 to 1.0 wt% (region B), the weight gain gradually increased and the volume fraction of tetragonal ZrO_2 decreased with increasing the Nb-content showing the effect of heat-treatment. The oxides were mainly of columnar structures. Nb-containing precipitate [$Zr(NbFe)_2$] were observed even in the 0.3 wt% Nb alloy.

In the high Nb-contents from 1.0 to 5.0 wt% (region C), the corrosion rates of the alloys were very sensitive to the heat-treatment showing the quite different corrosion behavior depending on the annealing condition. The samples annealed at 570 °C showed much lower corrosion rate with higher volume fraction of tetragonal ZrO_2 in the oxide than those annealed at 640 °C.

On the basis of the effect of soluble Nb in α matrix, Nb precipitate, and phase on the corrosion, it is suggested that the equilibrium Nb concentration in the α matrix would be a more dominant factor than the Nb-containing precipitate, β phases (β_{Nb} or β_{Zr}) and supersaturated Nb concentration in the enhancement of corrosion resistance of Zr–*x*Nb alloys.

Acknowledgements

This project has been carried out under the Nuclear Fuel R&D program by KAERI.

References

[1] G.P. Sabol, G.R. Kilp, M.G. Balfour, E. Roberts, ASTM STP 1023 (1989) 227.
[2] J.P. Mardon, G. Garner, P. Beslu, D. Charquet, J. Senevat, Proceedings of the 1997 International Topical Meeting on LWR Fuel Performance, Portland, Oregon, 2–6 March 1997, p. 405.
[3] H. Anada, K. Takeda, S. Hagi, T. Murata, A. Oe, T. Miyashita, Proceedings of the 2000 International Topical Meeting on LWR Fuel Performance, Park City, Utah, 10–13 April 2000.
[4] V.F. Urbanic, R.W. Gilbert, IAEA Technical Committee Meeting on Fundamental Aspects of Corrosion of Zr-based Alloys for Water Reactor Environments, Portland, Oregon, 11–15 September, 1989, p. 262.
[5] V.F. Urbanic, M. Griffith, ASTM STP 1354 (2000) 641.
[6] G.P. Sabol, R.J. Comstock, U.P. Nayak, ASTM STP 1354 (2000) 525.
[7] S. Banerjee, S.J. Vijayakar, R. Krishnan, J. Nucl. Mater. 62 (1976) 229.

[8] S.A. Aldridge, B.A. Chedle, J. Nucl. Mater. 42 (1972) 32.
[9] M.T. Javanovic, Y. Ma, R.L. Eadie, J. Nucl. Mater. 244 (1997) 141.
[10] T. Isobe, Y. Matsuo, ASTM STP 1132 (1991) 346.
[11] D. Stewart, B.A. Hatt, J.A. Roberts, Brit. J. Appl. Phys. 16 (1965) 1081.
[12] C.E.L. Hunt, P. Niessen, J. Nucl. Mater. 38 (1971) 17.
[13] E.T. Hayes, A.H. Roberson, W.L. O'Brien, Trans. Am. Soc. Mat. 43 (1951) 888.
[14] B. Cox, C.E. Lundin, Proceedings of the USAEC Symposium on Zirconium Alloy Development, Castlaewood, Pleasanton, California, 12–14 November 1962, p. 9.
[15] A. Perovic, V. Perovic, G.C. Weatherly, G.R. Purdy, R.G. Fleck, J. Nucl. Mater. 199 (1993) 102.
[16] Y.H. Jeong, K.O. Lee, H.G. Kim, T.H. Kim, J. Nucl. Mater. 302 (2002) 9.
[17] J. Godlewski, J.P. Gros, M. Lambertin, J.F. Wadier, H. Weidinger, ASTM STP 1132 (1991) 416.
[18] F. Garzarolli, H. Seidel, R. Tricot, J.P. Gros, ASTM STP 1132 (1991) 395.
[19] H. Anada, B.J. Herb, K. Nomoto, S. Hagi, R.A. Graham, T. Kuroda, ASTM STP 1295 (1996) 74.
[20] Y.H. Jeong, J.H. Baek, S.J. Kim, H.G. Kim, H. Ruhmann, J. Nucl. Mater. 270 (1999) 322.